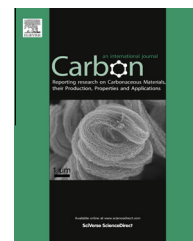


Available at [www.sciencedirect.com](http://www.sciencedirect.com)

SciVerse ScienceDirect

journal homepage: [www.elsevier.com/locate/carbon](http://www.elsevier.com/locate/carbon)

# One-step chemical vapor deposition synthesis of magnetic CNT–hercynite ( $\text{FeAl}_2\text{O}_4$ ) hybrids with good aqueous colloidal stability

Noé J. Morales <sup>a</sup>, Silvia Goyanes <sup>b</sup>, Claudio Chliotte <sup>c</sup>, Victoria Bekeris <sup>c</sup>, Roberto J. Candal <sup>a,d</sup>, Gerardo H. Rubiolo <sup>b,e,\*</sup>

<sup>a</sup> Instituto de Química Física de los Materiales, Medio Ambiente y Energía (INQUIMAE), CONICET-UBA, Ciudad Universitaria, C1428EHA Buenos Aires, Argentina

<sup>b</sup> Laboratorio de Polímeros y Materiales Compuestos, Departamento de Física, FCEyN, UBA-IFIBA (CONICET), Ciudad Universitaria, C1428EHA Buenos Aires, Argentina

<sup>c</sup> Laboratorio de Bajas Temperaturas, Departamento de Física, FCEyN, UBA, and IFIBA (CONICET), Ciudad Universitaria, C1428EHA Buenos Aires, Argentina

<sup>d</sup> Escuela de Ciencia y Tecnología, 3iA, Universidad Nacional de San Martín (UNSAM), Campus Miguelete, 25 de Mayo y Francia, 1650 San Martín, Provincia de Buenos Aires, Argentina

<sup>e</sup> Gerencia Materiales, Comisión Nacional de Energía Atómica, Avda Gral Paz 1499, B1650KNA San Martín, Argentina

## ARTICLE INFO

### Article history:

Received 17 February 2013

Accepted 28 April 2013

Available online 23 May 2013

## ABSTRACT

A multiwall carbon nanotube (MWCNT)/hercynite ( $\text{FeAl}_2\text{O}_4$ ) hybrid nanomaterial was synthesized by one-step chemical vapor deposition (CVD) using acetylene as precursor and  $\text{FeO}_x\text{-AlOOH}$  xerogel as catalyst. The hybrid material was composed by hercynite nanoparticles (diameter 10–50 nm) intimately attached to the walls of the MWCNTs. The diameter of the MWCNTs was related to particle size of the catalyst. The hybrid nanomaterial exhibited a characteristic magnetic behavior that can be considered as a combination of superparamagnetism and ferromagnetism, with a saturation magnetization of 5.7 emu/g at an applied field of 18 kOe and a coercivity of 520 Oe. The hybrid displayed a relatively low  $\text{pH}_{\text{ZPC}}$  (approx. 3.2) and formed very stable aqueous suspensions at pH 5.5. Controlled oxidation of the hybrid generated oxidized functional groups, as  $-\text{OH}$  and  $-\text{COOH}$ , and promoted the transformation of hercynite to hematite. Due to the high dispersibility of the hybrid in water, it presents an interesting potential as nanofiller for hydrophilic polymers.

© 2013 Elsevier Ltd. All rights reserved.

## 1. Introduction

Carbon nanotubes (CNTs) have been the focus of extensive research due to their outstanding electronic, mechanical, thermal, chemical properties and significant potential applications in nanoscience and nanotechnology [1]. Many recent studies focus on a new class of hybrid nanomaterials made from CNTs and inorganic glasses or ceramics, the

CNT–inorganic hybrids. In these hybrids, the CNTs are coaxially coated with the inorganic nanomaterial which gives it tunable electrical, magnetic and optical properties arising at the nanoscale (see for instance [2], and references therein). The various techniques for the synthesis of CNT–inorganic hybrids can be classified as *ex situ* and *in situ*. The *ex situ* technique first produces the inorganic component in the desired dimensions and morphology, then modifies with

\* Corresponding author. Fax: +54 11 6772 7362.

E-mail address: [rubiolo@cnea.gov.ar](mailto:rubiolo@cnea.gov.ar) (G.H. Rubiolo).

0008-6223/\$ - see front matter © 2013 Elsevier Ltd. All rights reserved.

<http://dx.doi.org/10.1016/j.carbon.2013.04.106>

functional groups either the inorganic nanoparticles (NPs) or the CNTs (or both) and finally attaches the inorganic component to the surface of CNTs by covalent, noncovalent, or electrostatic interactions. In contrast, the in situ technique carries out the synthesis of the inorganic component in the presence of pristine or functionalized CNTs, onto which the inorganic nanomaterial grows as particles, nanowires, or thin films.

A new potential application of CNT-inorganic hybrids was recently shown by Sue and co-workers [3] using an ex situ technique to prepare a CNT-clay nanoplate hybrid which can be effectively dispersed in aqueous solution down to individual level. They can also transfer the CNT-clay nanoplate hybrid from the aqueous dispersion to organic solvents by a drying redispersion process and then prepare a good quality epoxy/CNT composite which exhibits greatly improved modulus and strength at low nanotube loadings without compromising the strain at failure. No slippage or pull-out of the CNTs from the epoxy matrix was observed. Another kind of in situ technique has been addressed by Tian et al. [4] and Kudas et al. [5] to obtain micro/nanoscale hybrid reinforcements with a network structure where the CNTs are homogeneously dispersed and bond strongly with micro sized  $\text{Al}_2\text{O}_3$  powder. Their work focuses on synthesis of CNTs by chemical vapor deposition (CVD) process using micro sized alumina particles decorated with Ni NPs as catalyst. This catalyst is prepared through in situ process by using nickel salt and aluminum powder which are then calcinated at 900 °C.

The sol-gel technique is often the process for producing the catalyst used to synthesize multi-wall carbon nanotubes (MWCNTs) by CVD [6]. The porous nature of the matrix formed by sol-gel process provides the sites for nucleation of metal oxide NPs and the channels where carbonaceous species can flow. After synthesis, undesirable sideproducts, such as pieces of the ceramic matrix, remains attached to the CNTs. This system looks like the micro/nanoscale hybrids reported in references [4,5]. However the size of these ceramic particles is variable and can be potentially reduced to the nanometer size depending of the porosity of the matrix and also perhaps of the particle size of the calcinated xerogel [7].

The aim of this paper is to show the morphological characteristics and properties of the hybrid resulting from the synthesis of CNTs using a  $\text{FeO}_x\text{-AlOOH}$  xerogel obtained by the sol-gel method. The advantage of this one step synthesis is the easy and economical preparation of a nanocomposite material that combines the mechanical properties of CNTs, due to their large aspect ratio, with the hardness of a ceramic (hercynite) and the magnetic properties of iron NP. The appropriate combination of such properties would lead to a material with superior quality as filler for synthetic or natural polymers.

## 2. Experimental

Mesoporous aluminum oxide containing iron oxide (calcinated xerogel) was prepared by a sol-gel method following a protocol reported before for the synthesis of Fe-SiO<sub>2</sub> system [8]. Briefly, 5.51 g of aluminum tri-sec-butoxide (Aldrich) was mixed with 7.5 mL of a 1.5 M iron nitrate (Aldrich) aqueous solution and 5.0 mL of ethanol (Cicarelli) under continuing

**Table 1 – Summary of prepared samples: size, process stage and processing conditions.**

Sample name	Processing conditions
CTZ-A	Calcinated xerogel ( $50\ \mu\text{m} < \phi < 75\ \mu\text{m}$ )
CTZ-B	Calcinated-xerogel ( $\phi < 50\ \mu\text{m}$ )
CTZr-A	CTZ-A reduced in $\text{H}_2/\text{N}_2$ atmosphere
CTZr-B	CTZ-B reduced in $\text{H}_2/\text{N}_2$ atmosphere
NH-A	CNTs prepared from CTZ-A
NH-B	CNTs prepared from CTZ-B
NH-O1	NH-A heated 30 min at 600 °C, under 2.5 sccm $\text{O}_2$ , 180 torr
NH-O2	NH-A heated 30 min at 600 °C, under 5.0 sccm $\text{O}_2$ , 180 torr
NH-O3	NH-A heated 60 min at 650 °C, under 5.0 sccm $\text{O}_2$ , 180 torr

stirring, using 50  $\mu\text{L}$  of concentrated hydrofluoric acid (Merck) as catalyst for the hydrolysis and condensation reactions. A dark brown sol was obtained and dried for 6 days in two stages: first, 3 days in air at room conditions and second, 3 days under a 50 sccm flow of nitrogen at RH = 20%. Then, the obtained xerogel was calcinated at 450 °C under air atmosphere during 10 h. Prior to the synthesis of CNTs, the calcinated xerogel (named as catalyst CTZ) was ground in an agar mortar and sifted through ASTM No. 200 and ASTM No. 325 sieves. Then, two powders with different particle sizes were obtained. The sample name and the range of particle sizes for each powder are given in Table 1.

CNTs were synthesized by CVD using both CTZ-A and CTZ-B samples as catalyst. The CVD process, as reported in [8], consists of the following steps. First, the catalyst is placed into a combustion boat and introduced in a tubular oven. Second, the reduction reaction is made at 730 °C for 2 h under a 100 sccm flow of 10:90  $\text{H}_2/\text{N}_2$  with a total pressure of 180 torr (samples CTZr in Table 1). Thirdly, maintaining the temperature and  $\text{H}_2/\text{N}_2$  flow, 9.0 sccm of acetylene were introduced in the chamber during 1 h as carbon source for the growing of CNTs (samples NH in Table 1). Finally the system was cooled to room temperature under 100 sccm flow of  $\text{N}_2$ .

The sample NH-A was oxidized under controlled conditions to purify the CNTs and to introduce some functional groups at the surface. The samples were place in the tubular oven an expose to different oxygen flows as indicated in Table 1.

The  $\text{C}_2\text{H}_2$  conversion and carbon yield in the reaction was calculated based on Ref. [9]:

Carbon conversion:P

$$Q = [n_{\text{C}}/2 \times n_{\text{C}_2\text{H}_2}] \times 100\% \quad (1)$$

$$Q = \{[(M_{\text{tot}} - M_{\text{cat}}) \div 12] / [2 \times \text{flowrate (L/min)} \times \text{time (min)} \div 24.0 \text{ (L/mol)}]\} \times 100\% \quad (2)$$

Carbon yield:

$$Y = [(M_{\text{tot}} - M_{\text{cat}}) / M_{\text{cat}}] \times 100\% \quad (3)$$

where  $n_{\text{C}}$  is the number of moles of carbon and the  $n_{\text{C}_2\text{H}_2}$  is the number of moles of acetylene;  $M_{\text{tot}}$  is the mass of catalyst plus the mass of carbon entities and  $M_{\text{cat}}$  is the mass of catalyst.

The synthesized nanomaterials were characterized morphologically by scanning electron microscopy (SEM, FEG-SEM Zeiss Supra 40), and structurally by transmission electron microscopy (TEM, Philips EM 301). The crystalline structure was determined by X-ray diffraction (XRD, Siemens D 5000) using Cu-K $\alpha$  radiation. The thermal response was determined by thermogravimetry analysis (TGA, Shimadzu TGA-51) and differential thermal analysis (DTA) performed under air atmosphere. The pore size distribution of calcinated xerogels was determined by N<sub>2</sub> adsorption with a Micromeritics ASAP 2020, using Non-Local Density Functional Theory (NLDFT) to model the adsorption branch of the N<sub>2</sub> isotherms at 77 K. Fourier transformed infrared (FTIR) spectroscopy (Nicolet 510 P FTIR) was used to detect the functional groups generated on the surface of CNTs. The zero point of charge (pH<sub>ZPC</sub>) of the different materials was determined by measuring the electrophoretic mobility at different pHs (Brookhaven Zeta-Plus). 10 mg/L suspensions of the powders in 1.0 mM KCL were prepared and the pH adjusted with HCl or KOH. Magnetization hysteresis loops were measured on all specimens at room temperature, in the magnetic field range –18 to 18 kG, using a commercial vibrating sample magnetometer (VSM) LakeShore 7407.

### 3. Results

#### 3.1. CNT yielding, structure and morphology of the systems

CNTs were synthesized using both types of powders, CTZ-A and CTZ-B. The yielding calculated from Eqs. (1) and (3) was 90.3% and 250% respectively in both cases. The milling of the catalyst prior to the CNT synthesis did not affect the yielding of the reaction.

Fig. 1 shows XRD patterns of catalyst powders and the products obtained at each stage of the CVD process. Hematite phase, Fe<sub>2</sub>O<sub>3</sub>, was found in the calcinated xerogels (CTZ-A or CTZ-B). The diffractograms of the reduced xerogel (CTZr-A or CTZr-B) displays typical features of  $\alpha$ -Fe and hercynite,

FeAl<sub>2</sub>O<sub>4</sub>. Hercynite is an iron-aluminate in which iron is present as Fe(II).

The diffraction pattern of samples NH-A and NH-B are quite similar, the diffraction peak at  $2\theta = 26^\circ$  is typical of CNTs confirming that the incorporation of a flow of N<sub>2</sub>/acetylene in the reactor leaded to the synthesis of CNTs. An intense signal from cementite,  $\alpha$ -Fe<sub>3</sub>C, phase between  $40^\circ$  and  $50^\circ$  is observed hiding the iron peak if any. This phase also contributes with a diffraction peak appearing at the right side of the hercynite peak at  $2\theta = 36.53^\circ$ .

Fig. 2a shows a high magnified SEM image of the CTZs powders. The particles are formed by aggregates of nanoparticles and display a porous structure. The powders displayed a type IV isotherm which indicates the presence of mesoporosity, with a BET surface area of 169 m<sup>2</sup>/g. NLDFT analysis of the isotherms revealed that the calcinated xerogel have a wide pore size distribution with diameters between 2 and 45 nm, with an average pore size of 11 nm and the most probable value of 6 nm. This mesoporosity agree with the porous size that can be observed in the SEM images (Fig 2a). Fig. 2b shows typical SEM images of the hybrid formed by attachment of hercynite nanoparticles (HNP) on the walls of the CNTs. In some cases the HNPs almost surrounded CNTs (see the circles in Fig. 2b). The multiwall character of the carbon nanotubes was inferred from the hollow internal channel and wall width as observed in the TEM micrograph of Fig. 2c, also the attached HNPs and the canal of the CNTs can be clearly seen. No serious damage on the tube wall around the contact area with the nanoparticles was observed.

Although the yielding and the structure of the CNTs obtained with both catalysts (CTZ-A and CTZ-B) were quite similar, a detailed analysis of SEM pictures indicates that the external diameter of the CNTs differ depending on the particle size of the catalyst powder. Fig. 3 shows a histogram of the external diameter of the CNTs obtained with each catalyst powder. It is clear that the CNTs present in system NH-A had, in average, a larger external diameter than those present in system NH-B. The sieving of the catalyst powder prior to the synthesis did not affect the composition of the hybrid,

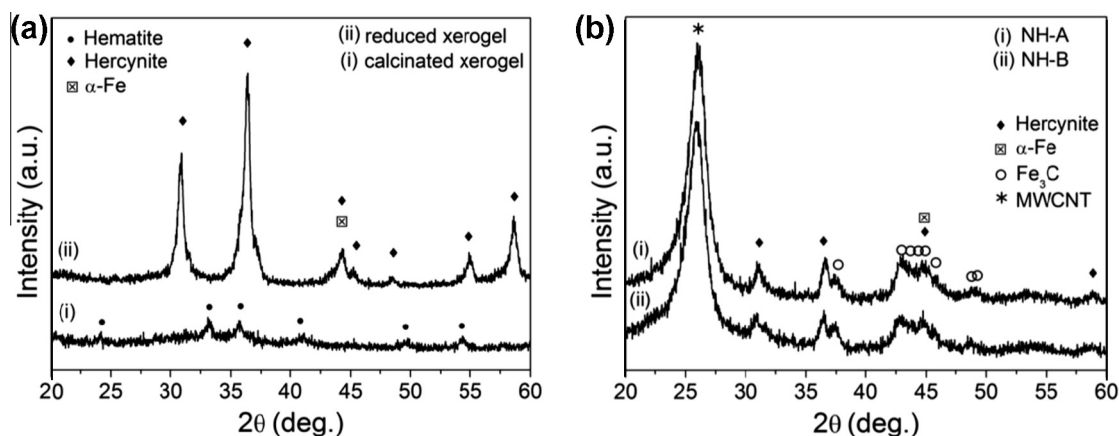


Fig. 1 – (a) XRD patterns for the calcinated xerogels (samples CTZ-A or CTZ-B), the reduced xerogel (samples CTZr-A or CTZr-B) and (b) the products from CVD process with catalyst CTZ-B or CTZ-A.

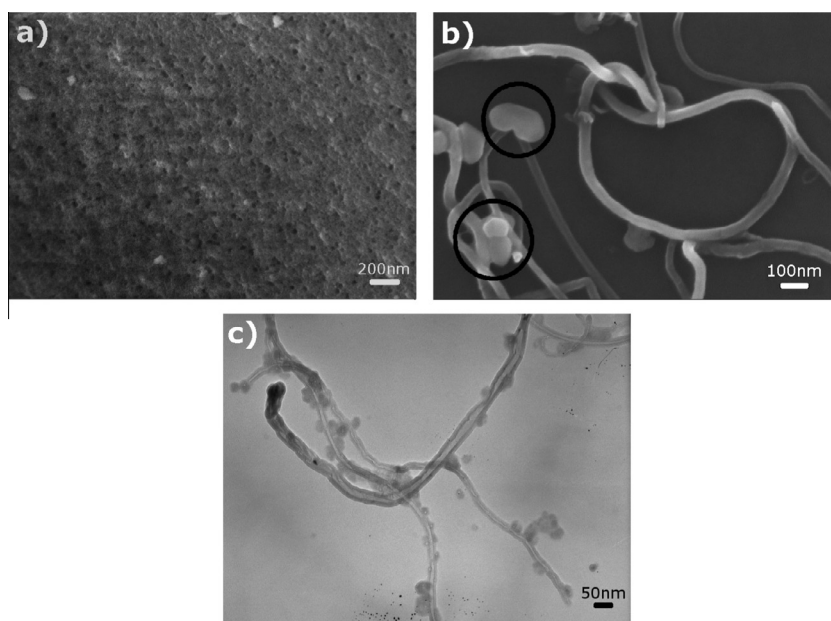


Fig. 2 – (a) Surface of calcinated xerogel, (b) synthesized CNT-hercynite hybrids; and (c) TEM image of the hybrids.

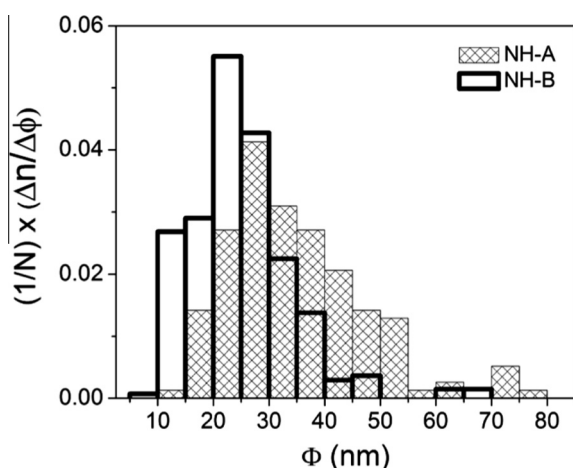


Fig. 3 – Distribution function of external CNT diameter using 200 data numbers for each hybrid.  $N$ : data numbers,  $\Phi$ : external diameter,  $n$ : number of data in  $\Delta\Phi$  interval.

but affected the morphology of the CNTs that grow from the sieved powder.

### 3.2. Thermal analysis

Fig. 4 shows the results of TGA and DTA analysis performed under air on samples NH-A and NH-B. As the temperature rises a slight increment of weight was observed in both systems, followed by a single and stepped weight loss centered at 580 °C. This weight loss can be assigned to the complete oxidation of the CNTs. The presence of only one step remarks the good quality of the synthesized CNTs. The remaining weight was about 20% in both cases and corresponds mostly to the ceramic that composes the hybrid. The DTA plots are

characterized by one endothermic feature that begins at 120 °C, over-imposed with an exothermic feature centered at 570 °C (NH-A) or 564 °C (NH-B). The exothermic feature can be consequence of the oxidation of CNTs to carbon dioxide, which also explains the steeped weight loss observed in the TG analysis. During TGA/DTA analysis of CTZr samples, only the endothermic feature and the slight increment in weight were observed. This effect can be related with oxidation of the reduced species present in the catalyst.

### 3.3. Controlled oxidation/purification process

The aim of this experiment was to eliminate the small amount of amorphous carbon that may contaminate the CNTs, and to create polar functional groups on their walls to increase their hydrophilicity. The CNTs present in the sample NH-O1 displayed the same aspect ratio as in the NH-A sample (Fig. 5a). After the thermal treatment the percentage of ceramic material was close to 40%, determined by TGA analysis (TGA not shown). A statistical analysis of the external CNT diameter using SEM images indicates that the oxidation process did not produce any appreciable change in diameter. Fig. 5a also shows changes in the morphology of the nanoparticles, that may be associated with changes in the composition and crystalline structure (see white circle). Fig. 5b shows the results of the XRD analysis of both NH-A and NH-O1 samples. From the comparison of both XRD patterns several changes can be noted in the XRD pattern of NH-O1 sample. First, there are two new diffraction peaks corresponding to hematite ( $\alpha$ -Fe<sub>2</sub>O<sub>3</sub>). Secondly, the CNT peak shape became thinner, probably as consequence of the loss of some carbonaceous material. Finally, the intensity of the hercynite and iron carbide peaks was reduced considerably. Further oxidation reduced even more the intensity of CNTs, hercynite and iron carbide diffraction peaks while increased the corresponding to hematite.



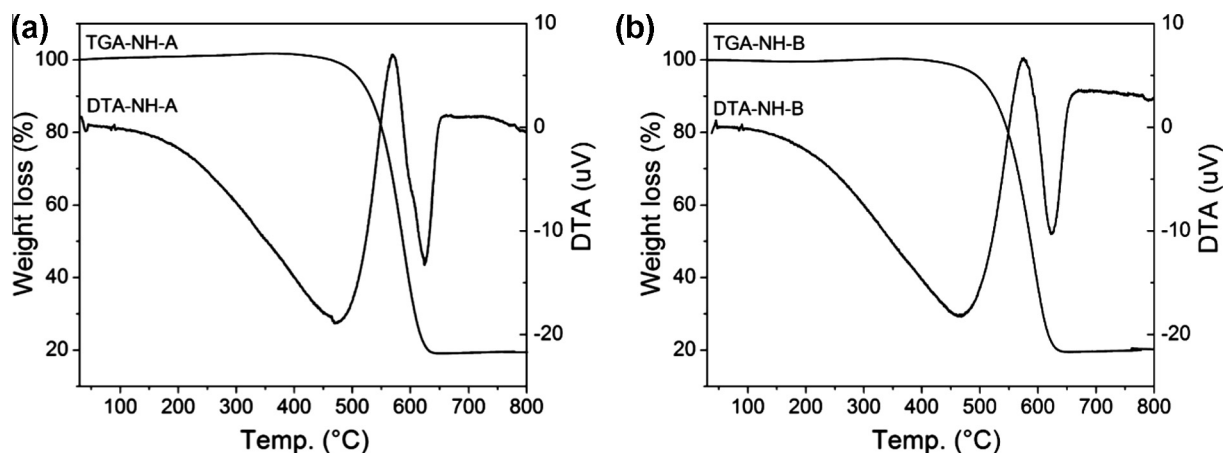


Fig. 4 – TGA and DTA of hybrids (a) NH-A and (b) NH-B.

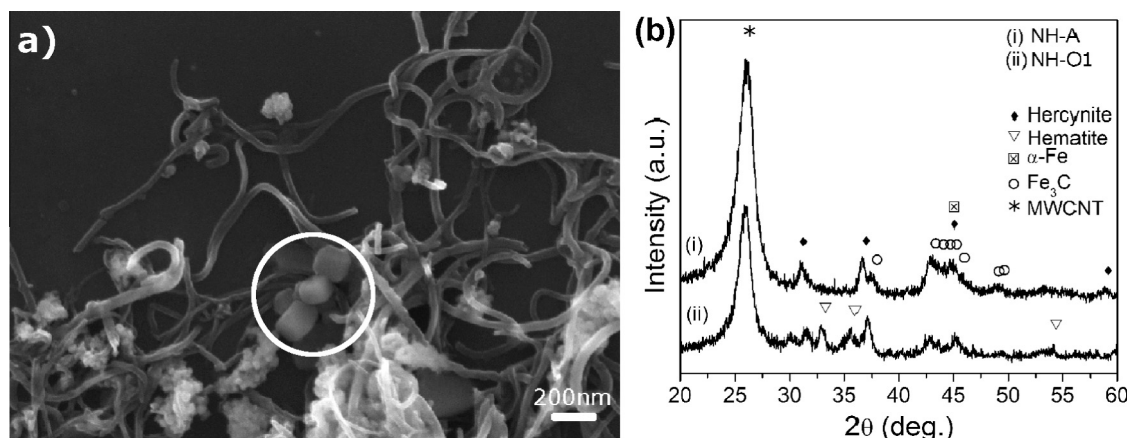
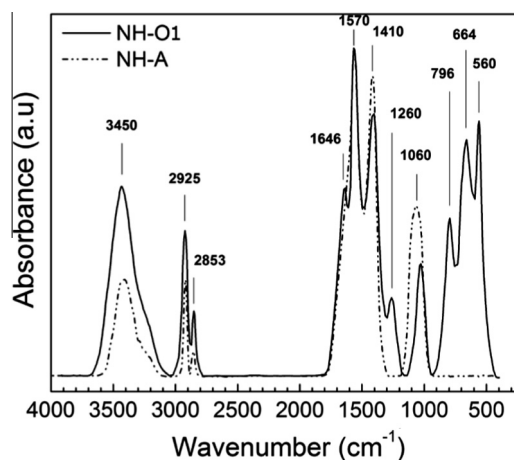


Fig. 5 – (a) SEM image of the hybrid in the NH-O1 sample. Hematite particles are remarked in the circle. (b) XRD pattern of hybrid material before (sample NH-A) and after (sample NH-O1) the purification/oxidation process.

Infrared spectroscopy was used to characterize the samples NH-A and NH-O1 in order to identify the CNTs and HNP surface functional groups. Fig. 6 shows the FTIR spectra of both samples. The spectra was first subtracted for the baseline and normalized at  $1570\text{ cm}^{-1}$ , the aromatic C=C structural vibrations of CNT backbone [10] are present in both spectra. The spectrum of sample NH-A displays characteristic features that are always present in raw MWCNTs indicating the presence of some oxygenated functional groups introduced during the synthesis process: a prominent broad band ( $3100\text{--}3600\text{ cm}^{-1}$ ) assigned to contributions from a variety of O–H stretching modes from hydroxyl or carboxyl groups; two bands at  $2925$  and  $2853\text{ cm}^{-1}$  ( $\text{CH}_x$  stretching) and a broad band between  $1000$  and  $1200\text{ cm}^{-1}$  (C–O from ethers, alcohols, anhydrides, lactones or carboxylic acids) [11,12]. One intriguing feature is the appearance of additional absorption in a band with structure located at  $1410\text{ cm}^{-1}$ ; most researchers are unable to assign this band to a particular functionality [11,13] but others related it to the presence of significant defects or disorder in CNT walls [14]. New IR bands appeared after the oxidation/purification process as shown by the

spectrum of sample NH-O1. There are several interesting changes between  $750$  and  $1300\text{ cm}^{-1}$ , the band at  $1060\text{ cm}^{-1}$  was reduced and shifted to  $1033\text{ cm}^{-1}$  together with the onset of two bands at  $796$  and  $1260\text{ cm}^{-1}$ . These three modes, together with the mode around  $1570\text{ cm}^{-1}$ , are close in frequency to the more characteristic IR modes calculated for chiral single wall carbon nanotubes [10]. These observations together with the reduction of the band at  $1410\text{ cm}^{-1}$  suggest that many of the functional groups seen in the spectrum of the NH-A sample may be attached to amorphous carbon or other carbonaceous fragments that were removed by the oxidation. The formation of new oxygenated functional groups can be seen in the onset of three bands at  $560$ ,  $664$  and  $1646\text{ cm}^{-1}$ , the first two can be assigned to the characteristic vibrations in hematite [15] and the third ascribed to the C=O stretching mode of quinone groups added preferentially to the ends of the tubes [13,16]. Also, there is an enhancement of the broad band at  $3450\text{ cm}^{-1}$  showing that the oxidation led to the addition of carboxylic acid and/or hydroxyl groups. Further oxidation of the hybrid was observed in samples NH-O2 and NH-O3. The proportion of hematite in the



**Fig. 6** – FTIR spectrum of hybrid nanomaterial before (NH-A) and after (NH-O1) the purification/oxidation process.

solid and the presence of polar functional groups follow the trend: NH-O1 < NH-O2 < NH-O3. The amount of CNTs in the hybrid decreases following the opposite trend.

### 3.4. Magnetic characterization

The magnetization curves recorded at room temperature for the samples CTZr-A and CTZr-B are presented in Fig. 7a. The magnetic behavior of both samples was similar, it can be seen that the samples were not saturated at high fields and shown remanent magnetization  $M_r$  and coercivity  $H_c$  greater than zero. This phenomenon can be considered a combination of superparamagnetic and ferromagnetic behaviors [17]. After CNT growth, there is an increment in the magnetization at a fixed applied field for the NH-A sample compared to the CTZr-A sample but this increment is nearly zero when the NH-B and CTZr-B samples are compared (Fig. 7b). The same behavior is observed in  $M_r$  but not in  $H_c$ . The highest magnetization measured is 5.7 emu/g at 18 kOe applied field in the NH-A sample while is 3.8 emu/g in the NH-B. These results indicate that the grinding and sieving of the catalysts before CNT synthesis also affects the magnetic behavior of the hybrid nanomaterial.

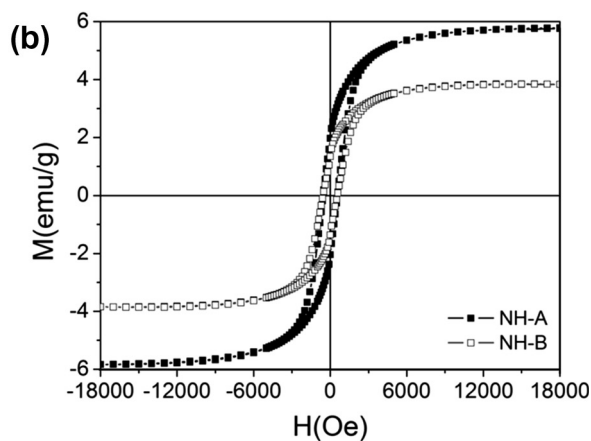
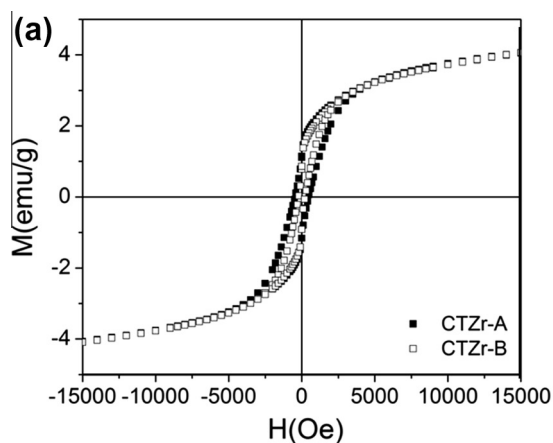


**Fig. 7** – Magnetic hysteresis loop of (a) reduced catalyst and (b) hybrid nanomaterials.

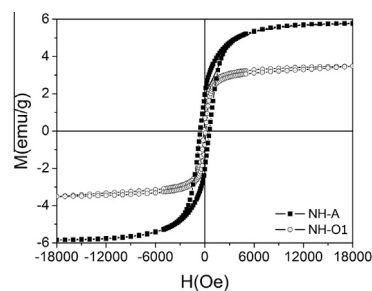


**Fig. 8** – Magnetization curves of the hybrids before (NH-A) and after (NH-O1) purification/oxidation process.

Partial oxidations of the NH-A sample also modify the magnetic properties of the hybrid. The sample NH-O1 displays demagnetization and loses the ferromagnetic contribution leaving in evidence the superparamagnetic behavior (Fig. 8).

### 3.5. Colloidal stability

To examine the colloidal stability of the as-synthesized CNT-hercynite hybrid (sample NH-A) and the oxidized hybrid (sample NH-O1) nanomaterials, they were dispersed in water as can be seen in Fig. 9a. During the dispersion, ultrasonic vibration was applied for 15 min. While the NH-O1 sample was stable only for 4 days (Fig. 9b), the sample NH-A remains stable for at least 3 weeks at room temperature.

Fig. 10 shows the electromobility of the NH-A hybrid and oxidized samples, it can be seen that the electromobility at the pH of work (5.5) decreases with the degree of oxidation. The pH of zero point charge ( $pH_{ZPC}$ ) of the hybrid, before and after controlled oxidation, is obtained from the data in Fig. 10 and displayed in Table 2. The results indicate that the  $pH_{ZPC}$  of the NH-A hybrid was far more negative than the pH of the suspension (5.5). The  $pH_{ZPC}$  of the oxidized samples increased with the oxidation time, being close to the hematite measured under similar conditions [18].

## 4. Discussion

The information obtained from XRD analysis (Fig. 1a) and the magnetic hysteresis loops (Fig. 7a) indicates that just after

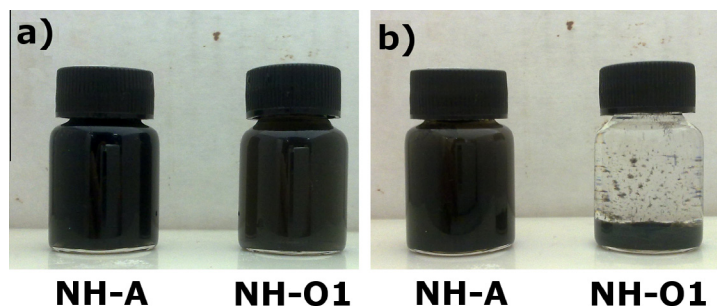


Fig. 9 – Dispersions of the NH-A and NH-O1 powders in water at pH 5.5 (GGG g/mL): (a) start time and (b) after 4 days.

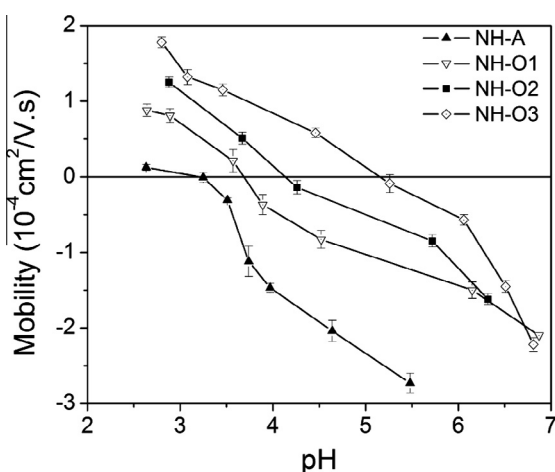


Fig. 10 – Electromobility of hybrid before (NH-A) and after purification/oxidation process. The preparation conditions are described in Table 1.

Table 2 –  $\text{pH}_{\text{ZPC}}$  of the hybrid before and after controlled oxidation.

Sample	NH-A	NH-O1	NH-O2	NH-O3
$\text{pH}_{\text{ZPC}}$	3.2	3.8	4.2	5.4

reduction (samples CTZr) the catalyst, independently of the powder mesh, is composed by a porous hercynite layer containing  $\alpha$ -iron nanoparticles and a core of incomplete reduced porous hercynite containing  $\text{Fe}_3\text{O}_4$  nanoparticles. We arrived to this description because: (i) hercynite is a paramagnetic material with very low magnetization at room temperature [19] then, the external layer with the  $\alpha$ -iron nanoparticles isolated in the hercynite matrix provides the superparamagnetic contribution to the magnetic hysteresis loop [20] and the characteristic XRD pattern of these catalysts; and (ii) the magnetic properties of solid solutions of  $\text{Fe}_3\text{O}_4$  and  $\text{FeAl}_2\text{O}_4$  show high magnetization moments and Curie temperatures [21] which could explain the ferromagnetic behavior observed in the CTZr samples. The thickness of the layer of catalyst containing  $\alpha$ -iron nanoparticles likely depends on the penetration of hydrogen inside the catalyst particles, which

depends on the microstructure of the particles (porosity, surface area, etc.) being independent of the particle diameter. Consequently, as the catalyst particle size decreases, the amount of  $\alpha$ -iron nanoparticles per volume unit should increase. However this effect is not observed in the magnetization of the samples CTZr (see Fig. 7a) probably because the difference in particle size is not large enough.

After CNT growth the particles of the reduced catalyst are fragmented to a nanometric size (see Fig. 2b and c), independently of the initial particle size. This fragmentation is due to the stress produced by the growth of CNTs, which may occur firstly inside the porosity of the external layer of the catalyst. The fragmentation creates new fresh surfaces which can be accessed by the gases of reduction and synthesis. Then part of the previously inactive Fe(II) and Fe(III) may become reduced and carburized at the same time. The reduction of iron cations with  $\text{H}_2$  may lead to the production of more Fe NPs which become a secondary site for CNT growth, otherwise a cementite nanoparticle appears. This process will induce a progressive fragmentation of the reduced catalytic particles under the constraints of “secondary” growing CNTs and the increase, during the same period, of cementite proportion as shown by the XRD spectrum in Fig. 1b. It is interesting to underline that this growth mode with successive liberations and activation of active sites by fragmentation of the reduced particles can explain why the CNT yielding is independent of the catalyst particle size. However, the difference in the outer diameter of the CNTs observed among the samples NH-A and NH-B (Fig. 3) implies that the total number of active  $\alpha$ -iron sites, both primary and secondary, were lower in the NH-A sample. This phenomenon is likely a consequence of the higher area expose to reduction gases in sample NH-B, where the initial particles are smaller than in sample NH-A. Consequently, in sample NH-A the excess carbon is deposited on the external walls of the already formed CNTs increasing its external diameter.

The original CNT growth reported herein leads to regular consumption of the iron nanoparticles, encapsulated inside the growing nanotubes, and the concomitant presence of  $\text{Fe}_3\text{C}$  nanoparticles inside the porosity of the remnant catalyst nanoparticles. Cementite nanoparticles encapsulated in carbon shell have shown superparamagnetic behavior at room temperature [22]. Then, the magnetic behavior of samples NH-A and NH-B can be considered to the ceramic nanoparticles attached to the CNTs and whose structure consists of an

incomplete reduced hercynite matrix containing  $\text{Fe}_3\text{C}$  nanoparticles. Because the fresh surface created in sample NH-A is larger than in sample NH-B, it is reasonable to expect a greater amount of cementite nanoparticles per unit volume in the first sample and consequently a greater magnetization as shown in Fig. 7b. Finally, the oxidation of the NH-A sample forms hematite ( $\alpha\text{-Fe}_2\text{O}_3$ ) and alumina (either amorphous or forming a solid solution with hematite), being hematite a weak ferromagnetic material at room temperature [23] and the second is not magnetic [24]. So, the magnetic hysteresis loop of sample NH-O1 loses the ferromagnetic contribution of the matrix and displays only a superparamagnetic behavior with a lower magnetization than sample NH-A (see Fig. 8).

Additionally, the FTIR results are consistent with this description of the ceramic material attached to the CNTs. In sample NH-A, the  $\text{Fe}_3\text{C}$  nanoparticles shield the hercynite matrix from the infrared light and therefore hides the absorption bands. After oxidation, the surface of the ceramic nanoparticles attached to the CNTs is rebuilt and the magnetic nanoparticles remain inside. Now, the absorption bands of the Fe–O functional groups in the hematite appear.

Unlike prior thought, the oxidized hybrid aqueous dispersion is less stable than that of as-synthesized CNT–hercynite hybrid although the chemical oxidation reaction modifying the CNT surface to possess carboxylic acid ( $-\text{COOH}$ ) or carboxylic anion ( $-\text{COO}^-$ ) groups [25]. An explanation could be found in the interfacial chemistry of the ceramic material attached to the CNTs. The  $\text{pH}_{\text{ZPC}}$  is an important guide to these interfacial properties. As showed in Table 2 the  $\text{pH}_{\text{ZPC}}$  of the hybrid is close to 3.2 while for NH-O1 is 3.8. Further oxidation even increases the  $\text{pH}_{\text{ZPC}}$ . This fact helps to explain the higher stability of NH-A in water when compare with NH-O1. The farther the pH from the  $\text{pH}_{\text{ZPC}}$ , more negatively is the electromobility so more stable is the suspension. The  $\text{pH}_{\text{ZPC}}$  of CNTs is close to 4.5 [26], this value cannot explain the  $\text{pH}_{\text{ZPC}}$  value of the hybrid. The hybrid  $\text{pH}_{\text{ZPC}}$  may be consequence of the presence of iron carbide surrounding the hercynite particles. To our knowledge there are no data available for the  $\text{pH}_{\text{ZPC}}$  of the cementite but, we propose here a way to get an estimated value by using an empirical correlation published in a very interesting paper devoted to measure the  $\text{pH}_{\text{ZPC}}$  of various metal carbides powders as NbC, WC, SiC and TiC [27]. The empirical correlation links the  $\text{pH}_{\text{ZPC}}$  values of those carbides with their metal–carbon bond strength, then taking the metal–carbon bond strength for cementite as the cohesive energy obtained by ab initio calculations (568 kJ/mol [28]) a value of  $\text{pH}_{\text{ZPC}} \cong 3.6$  can be estimated from that correlation. This value is close to that obtained for the hybrid (3.2). In the case of oxidized hybrid, FTIR and XRD results suggest that the nanoparticles are only partially coated by cementite, and hematite became an important phase. Coincidentally the  $\text{pH}_{\text{ZPC}}$  of NH-O1 moved to higher values getting closer to that of hematite (5.5–8 depending on measurement conditions). The  $\text{pH}_{\text{ZPC}}$  of the oxidized system is close to that of the suspension and consequently the stability of the water dispersion is lower.

The high conductivity, small diameter, high aspect ratio and super mechanical strength of MWCNTs make them an excellent option to create conductive composites for high-performance electromagnetic interference (EMI) shielding

materials at low filler concentration. Recently, they have been studied with various polymer matrix, including polystyrene (PS) [29], epoxy [30], poly(methyl methacrylate) (PMMA) [31], polyaniline (PANI) [29], polypyrrole (PPY) [29], polyurethane PU [30,32,33], etc., for the possible applications as effective and light weight EMI shielding materials. The EMI shielding properties are usually attributed to the capacity of these materials to reflect electromagnetic waves [34]. However, an interesting paper has reported the influence of the Fe metal catalyst inside of MWCNTs on the shielding efficiency (SE) in the near-field range of MWCNT–PMMA composites [35]. The authors showed that the contribution of absorption to the total EMI SE of the system is larger than that of reflection and the higher EMI SE of raw MWCNT–PMMA composites, compared to that of purified ones, mainly originates from the higher amount of Fe metal catalyst in the raw MWCNTs. As was recognized by the authors, this effect is negligible around of the dc electrical conductivity percolation threshold because the concentration of Fe catalyst particles is too low. Because the percentage of Fe contained in our hybrid is higher than in the material reported in [35], it can overcome the last drawback preserving the same EMI SE properties at lower filler fraction which is critical for real applications. Moreover, the high dispersibility and colloidal stability of the hybrid in water make them an excellent option by direct mixing with any kind of polymer which can be synthesized by water emulsion polymerization [36,37]. For example, by using the colloidal-physics method a CNT–hercynite/water-based PU composite may be synthesized, obtaining an ideal candidate to replace the current civil and military aircraft topcoats (based on PU). This coating should provide enough shielding properties to mitigate electrostatic build-up which can cause considerable damage to surrounding materials and electronics [38].

## 5. Conclusions

A MWCNT–hercynite hybrid nanomaterial has been successfully synthesized in a one step CVD process, using as catalyst iron oxide dispersed in a matrix of aluminum oxide prepared by sol–gel method. The catalyst was activated by reduction at 730 °C under  $\text{H}_2/\text{N}_2$  atmosphere, due to the formation of  $\alpha\text{-Fe}$  nanoparticles. The catalyst particle size, selected by sieving through ASTM No. 200 and between ASTM No. 200 and 325 sieves, did not affect the composition of the hybrid which was made up of 80% CNTs and 20% ceramic material (3 h of CVD process time). However, the mean diameter of the CNTs increases as does the particle size of the catalyst. This result is consequence of the number of available catalytic sites (iron nanoparticles) on the surface of the catalyst particles. During CNT growing the particles of the catalyst are exposed to intense stress that produce its fracture in small nanoparticles that remains physically attached to the external walls of the CNTs. The new system is a hybrid composed mostly of CNTs and hercynite with minor quantities of iron (nanoparticles) and iron carbide. The components of the hybrid cannot be separated by physical methods. The hybrid nanomaterial shows a typical magnetic behavior, different of those displays for the isolated components. This behavior can be considered



a combination of superparamagnetism and ferromagnetism. Also, the hybrid is easily dispersed in water and the dispersion remains very stable for long time at room temperature. The stability of the water dispersions is consequence of the low  $pH_{ZPC}$  of the hybrid (3.2). Due to its properties the hybrid nanomaterial has an enormous potential in the preparation of composites with hydrosoluble polymers for EMI shielding applications, also recently, similar nanomaterials were tested as contrast agent with specific target for magnetic resonance imaging [39], or as reinforcement for network structures [4,5]. The advantage of our novel fabrication route, without any post-synthesis treatment, is its simplicity and low cost due to the “one-step” procedure, the high yielding and quality of the CNTs.

## Acknowledgements

The authors wish to acknowledge the support and collaboration of the following organizations: UBA (UBACYT Nos. 20020100100350 and 2002090100297) and CONICET PIP 2010-2012, PIP 11220090100699. The research leading to these results has received funding from the European Community's Seventh Framework Program (FP7/2007–2013) under Grant Agreement No. 213939.

## Appendix A. Supplementary data

Supplementary data associated with this article can be found, in the online version, at <http://dx.doi.org/10.1016/j.carbon.2013.04.106>.

## REFERENCES

- [1] Baughman RH, Zakhidov AA, de Heer WA. Carbon nanotubes – the route toward applications. *Science* 2002;297(5582):787–92.
- [2] Eder D. Carbon nanotube–inorganic hybrids. *Chem Rev* 2010;110:1348–85.
- [3] Sun D, Chu CC, Sue HJ. Simple approach for preparation of epoxy hybrid nanocomposites based on carbon nanotubes and a model clay. *Chem Mater* 2010;22:3773–8.
- [4] He CN, Tian F. A carbon nanotube–alumina network structure for fabricating epoxy composites. *Scr Mater* 2009;61:285–8.
- [5] Kudus MHA, Akil HMd, Mohamad H, Loon LE. Effect of catalyst calcination temperature on the synthesis of MWCNT–alumina hybrid compound using methane decomposition method. *J Alloys Compd* 2011;509:2784–8.
- [6] Dupuis A. The catalyst in the CCVD of carbon nanotubes – a review. *Prog Mater Sci* 2005;50:929–96.
- [7] Morales Mendoza N, Goyanes S, Chilotte C, Bekeris V, Rubiolo G, Candal R. Magnetic binary nanofillers. *Physica B* 2012;407(16):3203–5.
- [8] Escobar M, Moreno MS, Candal RJ, Marchi MC, Caso A, Polosecki PI, et al. Synthesis of carbon nanotubes by CVD: effect of acetylene pressure on nanotubes characteristics. *Appl Surf Sci* 2007;254:251–6.
- [9] Chen CM, Dai YM, Huang JG, Jehng JM. Intermetallic catalyst for carbon nanotubes (CNTs) growth by thermal chemical vapor deposition method. *Carbon* 2006;44(9):1808–20.
- [10] Eklund PC, Holden JM, Jishi RA. Vibrational modes of carbon nanotubes: spectroscopy and theory. *Carbon* 1995;33:959–72.
- [11] Mawhinney DB, Naumenko V, Kuznetsova A, Yates JT. Infrared spectral evidence for the etching of carbon nanotubes: ozone oxidation at 298 K. *J Am Chem Soc* 2000;122:2383–4.
- [12] Escobar M, Goyanes S, Corcuera MA, Eceiza A, Mondragón I, Rubiolo GH, et al. Purification and functionalization of carbon nanotubes by classical and advanced oxidation processes. *J. Nanosci Nanotechnol* 2009;9:6228–33.
- [13] Kim UJ, Furtado CA, Liu X, Chen G, Eklund PC. Raman and IR spectroscopy of chemically processed single-walled carbon nanotubes. *J Am Chem Soc* 2005;127:15437–45.
- [14] Branca C, Frusteri F, Magazu V, Mangione A. Characterization of carbon nanotubes by TEM and infrared spectroscopy. *J Phys Chem B* 2004;108:3469–73.
- [15] Du N, Xu Y, Zhang H, Zhai C, Yang D. Selective synthesis of  $Fe_2O_3$  and  $Fe_3O_4$  nanowires via a single precursor: a general method for metal oxide nanowires. *Nanoscale Res Lett* 2010;5:1295–300.
- [16] Acuña JJS, Escobar M, Goyanes SN, Candal RJ, Zanatta AR, Alvarez F. Effect of  $O_2^+$ ,  $H_2^++O_2^+$ , and  $N_2^++O_2^+$  ion-beam irradiation on the field emission properties of carbon nanotubes. *J Appl Phys* 2011;109:114317.
- [17] Viegas ADC, Geshev J, Dorneles LS, Schmidt JE, Knobel M. Correlation between magnetic interactions and giant magnetoresistance in melt-spun  $Co_{10}Cu_{90}$  granular alloys. *J Appl Phys* 1997;82:3047–53.
- [18] Kosmulski M. The pH-dependent surface charging and points of zero charge. V. Update. *J Colloid Interface Sci* 2011;353:1–15.
- [19] Dutta DP, Sharma G. Synthesis and magnetic behavior of spinel  $FeAl_2O_4$  nanoparticles. *Mater Sci Eng B* 2011;176:177–80.
- [20] Caizer C, Hrianca I. Dynamic magnetization of  $\gamma-Fe_2O_3$  nanoparticles isolated in an  $SiO_2$  amorphous matrix. *Eur Phys J B* 2003;31:391–400.
- [21] Pickart SJ, Turnock AC. Magnetic properties of solid solutions of  $Fe_3O_4$  and  $FeAl_2O_4$ . *J Phys Chem Solids* 1959;10:242–4.
- [22] Fan N, Ma X, Ju Z, Li J. Formation, characterization and magnetic properties of carbon-encapsulated iron carbide nanoparticles. *Mater Res Bull* 2008;43:1549–54.
- [23] Esmaeili E, Salavati-Niasari M, Mohandes F, Davar F, Seyghalkar H. Modified single-phase hematite nanoparticles via a facile approach for large-scale synthesis. *Chem Eng J* 2011;170:278–85.
- [24] Karakassides MA, Gournis D, Bourlinos AB, Trikalitis PN, Bakas T. Magnetic  $Fe_2O_3$ – $Al_2O_3$  composites prepared by a modified wet impregnation method. *J Mater Chem* 2003;13:871–6.
- [25] Lee J, Kim M, Hong CK, Shim SE. Measurement of the dispersion stability of pristine and surface-modified multiwalled carbon nanotubes in various nonpolar and polar solvents. *Meas Sci Technol* 2007;18:3707–12.
- [26] Singh BP, Samal S, Bhattacharjee S, Besra L. Characterization and dispersion of multiwalled carbon nanotubes (MWCNTs) in aqueous suspensions: surface chemistry aspects. *J Dispersion Sci Technol* 2012;7:1021–9.
- [27] Cerovic LJ, Milonjic SK, Todorovic MB, Trtanj MI, Pogozhev YS, Blagoveschenskii Y, et al. Point of zero charge of different carbides. *Colloids Surf A* 2007;297:1–6.
- [28] Dick A, Körmann F, Hickel T, Neugebauer J. Ab initio based determination of thermodynamic properties of cementite including vibronic, magnetic, and electronic excitations. *Phys Rev B* 2011;84:125101.
- [29] Wang Y, Jing X. Intrinsically conducting polymers for electromagnetic interference shielding. *Polym Adv Technol* 2005;16:344–51.
- [30] Li N, Huang Y, Du F, He X, Lin X, Gao H, et al. Electromagnetic interference (EMI) shielding of single-walled carbon nanotube epoxy composites. *Nano Lett* 2006;6:1141–5.

- [31] Kim HM, Kim K, Lee SJ, Joo J, Yoon HS, Cho SJ, et al. Charge transport properties of composites of multiwalled carbon nanotube with metal catalyst and polymer: application to electromagnetic interference shielding. *Curr Appl Phys* 2004;4:577–80.
- [32] Ma CCM, Huang YL, Kuan HC, Chiu YS. Preparation and electromagnetic interference shielding characteristics of novel carbon-nanotube/siloxane/poly-(urea urethane) nanocomposites. *J Polym Sci Part B Polym Phys* 2005;43:345–58.
- [33] Liu Z, Bai G, Huang Y, Ma Y, Du F, Li F, et al. Reflection and absorption contributions to the electromagnetic interference shielding of single-walled carbon nanotube/polyurethane composites. *Carbon* 2007;45:821–7.
- [34] Dhawan SK, Ohlan A, Singh K. Designing of nano composites of conducting polymers for EMI shielding. In: Reddy B, editor. *Advances in nanocomposites – synthesis, characterization and industrial applications*. Rijeka (Croatia): InTech; 2011. p. 429–82.
- [35] Kim HM, Kim K, Lee CY, Joo J, Cho SJ, Yoon HS, et al. Electrical conductivity and electromagnetic interference shielding of multiwalled carbon nanotube composites containing Fe catalyst. *Appl Phys Lett* 2004;84:589–91.
- [36] Grossiord N, Loos J, Koning CE. Strategies for dispersing carbon nanotubes in highly viscous polymers. *J Mater Chem* 2005;15:2349–52.
- [37] Cai D, Song M. Water-based polyurethane filled with multi-walled carbon nanotubes prepared by a colloidal-physics method. *Macromol Chem Phys* 2007;208:1183–9.
- [38] Zhao W, Li M, Peng HX. Functionalized MWNT-doped thermoplastic polyurethane nanocomposites for aerospace coating applications. *Macromol Mater Eng* 2010;295:838–45.
- [39] Yin M, Wang M, Miao F, Ji Y, Tian Z, Shen H, et al. Water-dispersible multiwalled carbon nanotube/iron oxide hybrids as contrast agents for cellular magnetic resonance imaging. *Carbon* 2012;50:2162–70.